

2

TECHNICAL REPORT BRL-TR-3140

BRL

DTIC FILE COPY

AD-A226 433

**SPIKE-NOSED PROJECTILES:
COMPUTATIONS AND DUAL FLOW MODES
IN SUPERSONIC FLIGHT**

AMEER G. MIKHAIL

AUGUST 1990

DTIC
ELECTE
SEP 11 1990
S E D
Cs

APPROVED FOR PUBLIC RELEASE; DISTRIBUTION UNLIMITED.

U.S. ARMY LABORATORY COMMAND

**BALLISTIC RESEARCH LABORATORY
ABERDEEN PROVING GROUND, MARYLAND**

NOTICES

Destroy this report when it is no longer needed. DO NOT return it to the originator.

Additional copies of this report may be obtained from the National Technical Information Service, U.S. Department of Commerce, 5285 Port Royal Road, Springfield, VA 22161.

The findings of this report are not to be construed as an official Department of the Army position, unless so designated by other authorized documents.

The use of trade names or manufacturers' names in this report does not constitute indorsement of any commercial product.

UNCLASSIFIED

REPORT DOCUMENTATION PAGE			Form Approved OMB No. C704-0188	
<small>Public reporting burden for this collection of information is estimated to average 1 hour per response, including the time for reviewing instructions, searching existing data sources, gathering and maintaining the data needed, and completing and reviewing the collection of information. Send comments regarding this burden estimate or any other aspect of this collection of information, including suggestions for reducing this burden, to Washington Headquarters Services, Directorate for Information Operations and Reports, 1215 Jefferson Davis Highway, Suite 1204, Arlington, VA 22202-4302, and to the Office of Management and Budget, Paperwork Reduction Project (0704-0188), Washington, DC 20503</small>				
1. AGENCY USE ONLY (Leave blank)	2. REPORT DATE August 1990	3. REPORT TYPE AND DATES COVERED Final, Jan 89 - Dec 89		
4. TITLE AND SUBTITLE SPIKE-NOSED PROJECTILES: COMPUTATIONS AND DUAL FLOW MODES IN SUPERSONIC FLIGHT		5. FUNDING NUMBERS 1L162618AH80 62618A-00-001 AJ		
6. AUTHOR(S) Ameer G. Mikhail				
7. PERFORMING ORGANIZATION NAME(S) AND ADDRESS(ES)		8. PERFORMING ORGANIZATION REPORT NUMBER		
9. SPONSORING / MONITORING AGENCY NAME(S) AND ADDRESS(ES) Ballistic Research Laboratory ATTN: SLCBR-DD-T Aberdeen Proving Ground, MD 21005-5066		10. SPONSORING / MONITORING AGENCY REPORT NUMBER BRL-TR-3140		
11. SUPPLEMENTARY NOTES The help given by Dr. N.R. Patel in the early stage of code adoption and initial problem set-up is gratefully acknowledged.				
12a. DISTRIBUTION / AVAILABILITY STATEMENT Approved for public release; distribution is unlimited		12b. DISTRIBUTION CODE		
13. ABSTRACT (Maximum 200 words) This study was made to assess the capability of a Computational Fluid Dynamic (CFD) method to adequately determine the aerodynamic coefficients for the unusual configurations of sharp-edged, spike-nosed projectiles that are of interest to the US Army. McCormack's time-dependent, explicit scheme was used for the full Navier-Stokes equations in a zonal gridding topology. Three configurations were computed at Mach = 1.72 and zero angle of attack. The results are compared against wind tunnel data. The flow fields computed are in qualitative agreement with wind tunnel schlieren photographs, and the computed drag coefficients are within two percent of the wind tunnel measurements. Two important issues are faced: (1) the always existing possibility of a dual flow mode and which one will occur under specific flow conditions; and (2) observed role of the turbulence level and numerical model in affecting flow separation and, thus, influencing a particular flow mode to be predicted. This study demonstrates the successful application of the present approach to these unusual configurations and, thus, leads the way to further application for more complex configurations, such as those with booms and fins.				
14. SUBJECT TERMS Numerical Computations Navier-Stokes Equations Supersonic Aerodynamics		Spike-Nosed Projectiles Dual Flow Modes Blunt Bodies		15. NUMBER OF PAGES 42
				16. PRICE CODE
17. SECURITY CLASSIFICATION OF REPORT UNCLASSIFIED	18. SECURITY CLASSIFICATION OF THIS PAGE UNCLASSIFIED	19. SECURITY CLASSIFICATION OF ABSTRACT UNCLASSIFIED	20. LIMITATION OF ABSTRACT UL	

UNCLASSIFIED

INTENTIONALLY LEFT BLANK.

TABLE OF CONTENTS

	<u>Page</u>
LIST OF FIGURES	v
ACKNOWLEDGMENTS	vii
1 INTRODUCTION	1
2 ABOUT THE TEST CASES	2
3 GOVERNING EQUATIONS	2
3.1 Turbulence Model	4
4 ABOUT THE CODE, GRID, AND COMPUTATIONS	5
4.1 The Code	5
4.2 Boundary Conditions	6
4.3 Initial Conditions	6
4.4 The Grid	6
5 RESULTS	7
5.1 Configuration 1	7
5.2 Configuration 2	8
5.3 Configuration 3	9
5.4 Grid Size Effect	9
6 SUMMARY AND CONCLUSIONS	10
7 REFERENCES	33
LIST OF SYMBOLS	35
DISTRIBUTION LIST	37

Accession For	
NTIS CHAM	<input checked="" type="checkbox"/>
DTIC TAB	<input type="checkbox"/>
Unannounced	<input type="checkbox"/>
Justification	
By	
Distribution/	
Availability Codes	
Dist	Avail and/or Special
A-1	

Intentionally left blank.

LIST OF FIGURES

<u>Figure</u>	<u>Page</u>
1 Wind tunnel model of the first projectile configuration	11
2 Wind tunnel model of the second projectile configuration	12
3 Wind tunnel model of the third projectile configuration	13
4 Typical flow features for the low- and high-drag modes	14
5 Grid zones and computational domain for the spike-nosed projectiles	15
6 Zonal grid for the first projectile configuration	16
7 Zonal grid for the second projectile configuration	17
8 Zonal grid for the third projectile configuration	18
9 Mach number contours for the low-drag mode for Configuration 1	19
10 Mach number contours for the high-drag mode for Configuration 1	20
11 Details of Mach number contours near the spike tip (low-drag, Configuration 1) . .	21
12 Details of Mach number contours near the spike tip (high-drag, Configuration 1) . .	22
13 Details of Mach number contours near the facing shoulder (low-drag, Configuration 1)	23
14 Details of Mach number contours near the facing shoulder (high-drag, Configuration 1)	24
15 Forebody drag coefficient comparison for Configuration 1 (low-drag mode)	25
16 Mach number contours for Configuration 2 (low-drag mode)	26
17 Mach number contours for Configuration 2 (high-drag mode)	27
18 Forebody drag coefficient comparison for Configuration 2 (low-drag mode)	28
19 Mach number contours for Configuration 3 (low-drag mode)	29
20 Mach number contours for Configuration 3 (high-drag mode)	30

Intentionally left blank

ACKNOWLEDGMENTS

The help given by Dr. N. R. Patel in the early stage of code adoption and initial problem set-up is gratefully acknowledged.

Intentionally left blank.

1. INTRODUCTION

Spike-nosed configurations are used for projectile applications against armored targets where the spike is used as a stand-off distance causing microseconds of advance time between the time that the tip of the spike touches the armor and the time that the warhead (usually a shaped charge) detonates. Spike nose configurations are also used for a different purpose, namely reducing the drag for blunt reentry vehicles at hypersonic speeds when drag and heating are of major concern.

After World War II, a new generation of spike-nosed high explosive, anti-tank (HEAT) projectiles was developed in the U.S. and abroad. In the very early stage of development, during the late 1940s and early 1950s, spinning HEAT projectiles were examined; but it was quickly found that spin reduces the depth of penetration in the armor. Therefore, most spike-nosed projectiles, in the late 1950s and thereafter, were fin-stabilized and were provided with a tail boom and fins behind the shaped-charge warhead.

Many experimental studies were made for finned, spike-nosed projectiles. Some wind tunnel tests can be found, for example, in References 1 through 5. Some firing-range tests are reported in References 6 through 9. The U.S. Air Force, during the 1960-70s, extensively studied the unsteady front-shock flow phenomenon (the buzzing) for spike-nosed reentry vehicles at high speeds.¹⁰⁻¹² Also, the Air Force successfully computed the unsteady buzzing flow for these reentry configurations of interest.¹³⁻¹⁵

At present, for sharp-edged, spike-nosed projectiles of interest to the Army, there is no analytic or formal computational procedure that can be systematically used to predict the aerodynamics of such configurations. The Army has relied so far on direct wind tunnel tests followed by live firing of projectiles in the firing ranges. The present study was made to establish such a systematic, numerical, predictive technique. Therefore, validation of the predictive technique against range or wind tunnel data is of vital importance for assessing the numerical capability. Although the final objective is the application to finned, spike-nosed projectiles, this study, being a first step toward that goal, limited itself to unfinned, spike-nosed configurations in an attempt to focus on the spike-nosed flow with its complex features. These features include dual flow modes, large separation regions, and unsteadiness. By establishing that such flows can be systematically and successfully computed, the doors will be opened for future work to tackle similar configurations with added booms and fins.

The advances in the zonal gridding and overlapping techniques made this study possible for

the present sharp-edged configurations. This represents the first known application of computational fluid dynamics to Army spike-nosed projectile shapes.

2. ABOUT THE TEST CASES

Very few experimental results are available for unfinned, spike-nosed projectiles in contrast to those of finned ones for the reason stated earlier. For the sharp-edged configuration, only the wind tunnel tests of Platou¹⁶ are applicable. Also, some firing range data are available, but for configurations with a tripping ring.¹⁷ Very recent wind tunnel tests were made by Koenig, et al.,¹⁸ while this work was being completed, for very similar configurations with different spike lengths at Mach numbers between 0.8 to 1.5 and zero angle of incidence. Results of Reference 18 could be used for further validations in the future.

Three cases from Reference 16 were chosen. They are shown in Figures 1-3. The wind tunnel tests were made in 1950 at the Ballistic Research Laboratory supersonic wind tunnels at $M=1.72$ for angles $-10^\circ < \alpha < +10^\circ$. The Reynolds number was 4.86×10^6 per foot, $T_o=100^\circ \text{ F}$, and $P_o=1.26$ atmospheres. The model diameter is 2.5 inch for all three configurations. The first two configurations were reported not to have dual flow modes at this Mach number and range of α . The flow features of both modes are depicted in Figure 4. The third configuration was reported to have had the dual flow modes (the high-drag, open-flow mode and the low-drag, closed flow mode). However, the low-drag mode briefly occurred while increasing α and was captured on a schlieren photograph, but the drag force itself was not measured. The high-drag mode then persisted, while the lower drag mode could never be recovered again during the tests.¹⁶

3. GOVERNING EQUATIONS

The compressible, turbulent Navier-Stokes equations for axisymmetric and two-dimensional flow can be expressed¹⁹ in the following strong conservation form, in which the dependent variables ρ , u , v , and e are mass averaged, with e being the specific total energy, T being the temperature, ρ and p being mean density and pressure, respectively, and t denoting time:

$$\frac{\partial Q'}{\partial t} + \frac{\partial E'}{\partial x} + \frac{\partial F'}{\partial y} + \left(\frac{F'}{y} + \frac{H'}{y} \right) \beta = 0 \quad (1a)$$

where

$$\left. \begin{aligned}
 Q' &= \begin{pmatrix} \rho \\ \rho u \\ \rho v \\ \rho e \end{pmatrix} & E' &= \begin{pmatrix} \rho u \\ \rho u u + p - \tau_{xx} \\ \rho u v - \tau_{xy} \\ (\rho e + p)u - \tau_{xx}u - \tau_{xy}v + \dot{q}_x \end{pmatrix} \\
 F' &= \begin{pmatrix} \rho v \\ \rho u v - \tau_{xy} \\ \rho v v + p - \tau_{yy} \\ (\rho e + p)v - \tau_{xy}u - \tau_{yy}v + \dot{q}_y \end{pmatrix} \\
 H' &= \begin{pmatrix} 0 \\ 0 \\ -p + \sigma_+ \\ 0 \end{pmatrix} \\
 \tau_{xx} &= -2/3 (\mu + \epsilon) \nabla \cdot \underline{V} + 2(\mu + \epsilon) \frac{\partial u}{\partial x} \\
 \tau_{xy} &= (\mu + \epsilon) \left(\frac{\partial u}{\partial y} + \frac{\partial v}{\partial x} \right) \\
 \tau_{yy} &= -2/3 (\mu + \epsilon) \nabla \cdot \underline{V} + 2(\mu + \epsilon) \frac{\partial v}{\partial y} \\
 \tau_{\theta\theta} = \sigma_+ &= -2/3 (\mu + \epsilon) \nabla \cdot \underline{V} + 2(\mu + \epsilon) \frac{v}{y} \\
 \nabla \cdot \underline{V} &= \frac{\partial u}{\partial x} + \frac{\partial v}{\partial y} + \left(\frac{v}{y} \right) \beta \\
 \dot{q}_x &= -C_p \left(\frac{\mu}{Pr} + \frac{\epsilon}{Pr_t} \right) \frac{\partial T}{\partial x} \\
 \dot{q}_y &= -C_p \left(\frac{\mu}{Pr} + \frac{\epsilon}{Pr_t} \right) \frac{\partial T}{\partial y}
 \end{aligned} \right\} \quad (1b)$$

where μ is molecular viscosity, ϵ is the turbulent eddy viscosity, and $\beta = 1$ or 0 for axisymmetric and two-dimensional cases, respectively.

The air is assumed to be a perfect gas, satisfying the equation of state $p = \rho RT$, where R is the gas constant ($1,716 \text{ ft}^2/\text{sec}^2 \cdot ^\circ\text{R}$ for air). For the dependence of laminar viscosity on temperature, Sutherland's law was used:

$$\mu = 2.270 \frac{T^{3/2}}{T + 198.6} \times 10^{-8} \frac{\text{lb} \cdot \text{sec}}{\text{ft}^2} \quad (2)$$

The laminar and turbulent Prandtl numbers, Pr and Pr_t , were assumed constant with values of 0.72 and 0.9, respectively. The ratio of specific heats, γ , was also assumed constant and equal to 1.4. C_v and C_p are specific heat capacities at constant volume and constant pressure, respectively:

$$C_v = 4290 \text{ ft}^2/\text{sec}^2 \cdot ^\circ\text{R},$$

and

$$C_p = 6006 \text{ ft}^2/\text{sec}^2 \cdot ^\circ\text{R} \text{ for air.}$$

The total energy per unit mass, e , is given by:

$$e = C_v T + (1/2) (u^2 + v^2).$$

In the $\xi - \eta$ computational plane, Equations 1a and b are transformed to the conservation law form, and the equations can be found, for example, in Reference 19.

3.1 Turbulence Model. Turbulence is modeled through the algebraic eddy-viscosity model of Baldwin and Lomax.²⁰ This model employs the two-layer concept (inner and outer). The inner layer is near the walls and is modeled as:

$$\epsilon_t = \rho l^2 |\omega|, \quad (3a)$$

$$l = ky \left(1 - \exp \left(-\frac{y^+}{A^+} \right) \right) \quad (3b)$$

The magnitude of the vorticity $|\omega|$ is:

$$|\omega| = \left| \frac{\partial u}{\partial y} - \frac{\partial v}{\partial x} \right| \quad (3c)$$

where

$$y^+ = \left(\frac{\rho_w |\omega_w|}{\mu_w} \right)^{1/2} y \quad (3d)$$

The distance normal to the surface is y ; $A^+ = 26$; $k = 0.40$ is the von Karman constant; and the subscript w denotes values at the surface.

The model switches from the inner to the outer region at the smallest value of y for which the inner and outer values of the eddy-viscosity are equal (i.e., $\epsilon_i = \epsilon_o$). The ϵ for the outer layer is given by

$$\epsilon_o = \rho K C_{cp} F_{max} y_{max} F_{KLEB} \quad (3e)$$

where

$$F_{max} = y_{max} |\omega| \left(1 - \exp \left(\frac{-y^+}{A^+} \right) \right) \quad (3f)$$

The value of y at which F_{max} occurs is y_{max} .

$$F_{KLEB} = [1 + 5.5(C_{KLEB} y / y_{max})^6]^{-1} \quad (3g)$$

$$K = 0.0168, \quad C_{cp} = 1.6, \quad C_{KLEB} = 0.3 \quad (3h)$$

Due to the perpendicular surfaces of the spike surfaces at the nose tip and at the facing shoulder, the normal distance to the wall, y , in Equation 3 is difficult to assign.²¹ This problem was solved in Reference 21 by measuring the y along a 45° ray emanating from the point of intersection of the two perpendicular walls.

4. ABOUT THE CODE, GRID, AND COMPUTATIONS

4.1 The Code. The code was developed by Patel and Sturek¹⁹. It utilizes the familiar and robust, explicit, time-dependent method of McCormack. The code was vectorized and is run on a

Cray-XMP/48 Machine. The present computations were all run in serial arithmetic mode. The zonal grid and overlap provided in the code are represented by eight different available zones (which can be increased if so desired). The user prescribes the overlap between regions along one line of adjacent zones (interface). A global, uniform, time step was used herein against grid-varying time steps to simulate time-accurate solutions. The time step is determined from the Courant-Fredrick-Levy (CFL) condition, with a factor of about 0.6 being used as the Courant number.

4.2 Boundary Conditions. No-slip conditions are specified on all wall surfaces. The incoming flow conditions are assumed to be of uniform profiles with free-stream temperature of $T_\infty = 520 \text{ R}^\circ$, $p_\infty = 14.7 \text{ psi}$, $M_\infty = 1.72$.

The outgoing conditions at the end of the projectile were imposed as zero gradients parallel to the body axis direction.

The outer boundary conditions were imposed as nonreflective conditions, i.e., zero-gradient conditions along characteristic lines for all variables. The characteristic direction is determined from the local velocity and temperature. This approach allows setting the "outer" field close to the body without the penalty of any unnecessary approximations regarding shock reflection, or zero-gradient conditions.

At the symmetry line, ahead of the spike tip, a two-point, zero-gradient, boundary condition is imposed on the solved variables.

4.3 Initial Conditions. Computations were started using free-stream values everywhere in the domain. These values are for free stream velocity, pressure, and temperature. The density and specific total energy are computed accordingly, using the equation of state and the definition of the specific total energy.

4.4 The Grid. Three different grid zones were used in the computation. Those zones and the extent of the computational domain are depicted in Figure 5.

For the first configuration, the grids used for the three zones are (15x48), (26x39), and (21x25), respectively. The first and second arguments in the parentheses refer to the axial and radial directions, respectively. This grid has 2,259 total points and is equivalent to a (48x48) grid.

One restriction in the present grid overlapping technique is the requirement that no interpolation is allowed at the interface line between zones. Thus, each point on either side of any two zones must have exactly the same coordinates. This restriction represents some constraint in the flexibility of the grid distribution and may be alleviated in future development of the code. Meanwhile, to accommodate this restriction, one has to accept unnecessary clustering of points in some locations. Figure 6 shows the clustered points along lines parallel to the top body surface, where clustering is needed near the body to resolve the turbulent boundary layer. Figure 6 shows the overall grid distribution for the first projectile configuration.

The sharp cone spike configuration was also modeled using three zones, but with grid sizes of (15x39), (26x39), and (21x25), respectively. This grid totals 2,124 points, or the equivalent of a (46x46 mesh), and is depicted in Figure 7.

The third configuration was computed using zones of sizes (15x44), (21x35), and (31x35). This grid totals 2,480 points or (50x50), approximately. This grid for configuration 3 is given in Figure 8. The grids were generated using a simple algebraic (exponential) formula in each zone in both the axial and radial directions.

5. RESULTS

5.1 Configuration 1. The low-drag mode was obtained by straightforward computation, assuming the flow to be fully turbulent everywhere. Unsteadiness occurred in the computation, but, when the turbulence level was reduced to 0.2 of its value at each point, the flow became steady. The Mach contours are provided in Figure 9. Comparison with the schlieren photograph of Reference 16 indicated good agreement of flow features. The bow shock stand-off distance was $0.5 d_b$ as theoretically predicted, and the bow shock angle away from the body nose tip was about 40° , the same as can be determined from the schlieren. The computation converged satisfactorily after 4,000 time steps, although the code was later run to 12,000 steps to assure the stability of computations. The computer CPU time was 40 minutes on the Cray-XMP/48 for the 4,000 steps.

Several numerical experiments were made to obtain the high-drag mode, even though that mode was not confirmed during the tests of Reference 16. The high-drag mode was easily obtained by freezing (i.e., not updating) the turbulence level after 1,000 steps and by simultaneously relaxing the time step at each point to 0.6 of its local Courant time step value. The solution also converged satisfactorily after 6,000 time steps, using 60 minutes on the same computer. Figure 10 depicts the flow field as presented by the Mach contours for this high-drag mode.

Comparison between the local flow fields of the two modes near the spike tip is given in Figures 11 and 12, respectively. For the high-drag mode, there is an expansion fan near the tip, which is followed immediately by coalescence of compression waves facing the separation region. These compression waves coalesce into a shock which faces the facing shoulder of the projectile, thus raising the pressure behind it and also that on the facing wall. This higher pressure results in the higher drag of the projectile. Surprisingly, the corresponding flow detail near the facing shoulder differs very slightly for the two modes. It was expected that larger differences would be observed there. Figures 13 and 14 provide the details for those modes near the facing shoulder.

The forebody drag coefficient for the computed geometry (low-drag) was 0.337. The drag due to the rotating band, which is shown in Figures 1-3 but was not modeled in the computation, was estimated²² to be 2% of the total drag at $M = 1.72$. The computed drag is, therefore, provided as 0.344, while the wind tunnel measurement given in Reference 16 is 0.351 for the forebody drag. Reference 16 provides the net forebody drag without any reference to base drag corrections. The computation, thus, underpredicts the measurement by 2%. Considering the tunnel measurement accuracy, one can conclude that these flow results are very assuring and useful. This result is shown in Figure 15. For the high-drag mode, the computed drag coefficient was 0.402 and is provided as 0.410 when including the 2% rotating band effect. The high-drag mode, therefore, resulted in a 19% increase in drag over the low-drag mode.

5.2 Configuration 2. The high-drag mode was obtained first when the computation of Configuration 1 was repeated, assuming fully turbulent flow everywhere and no reduction in the turbulence level. The computation was slower in converging, requiring 7,000 time steps for satisfactory convergence.

To obtain the low-drag mode, which is the mode reported¹⁶ to occur, laminar flow and transition should be allowed to occur on the cone. Therefore, laminar flow was allowed on the cone, and transition was allowed to occur only along the middle third of the whole spike length. This was based on estimates of location of transition (local Reynolds number), which were evaluated using References 23 and 24. The low-drag mode was immediately obtained, but with slower convergence rate. Convergence required about 12,000 time steps, requiring 120 minutes on the Cray-XMP/48 Machine.

The two flow modes are depicted in Figures 16 and 17. In Figure 16, the flow seems to slide over the separated region of the spike, while in Figure 17, for the high-drag mode, there is a compression wave appearing at the beginning of the separated region, thus signifying flow path turning.

The forebody drag coefficient for the low-drag case was 0.314 (including the 2% rotating band drag), compared to 0.321 for the wind tunnel measurement. Again, computation is within 2% of the measurement. Figure 18 depicts the comparison in the drag value. The high-drag mode drag coefficient was computed as 0.397 (including the 2%) and, thus, is 26% higher than that of the low-drag mode. The high drag mode was not observed during the tests of Reference 16.

5.3 Configuration 3. The high-drag mode was obtained readily when the computation, similar to that for Configuration 1, was applied here. Fully turbulent flow everywhere with no reduction in turbulence level was applied. Computations required only 4,000 steps for satisfactory convergence.

Several numerical attempts were made to obtain the low-drag mode. It was found that, by imposing a 3.5% cross flow (i.e., $v = 0.035 V_\infty$) in the free stream in zone 1, the flow mode was readily obtained. This 3.5% cross flow falsely simulated a pseudo 2° angle of attack. Although this is not truly an angle-of-attack effect, the cross velocity is an influence that can be related to an angle of attack.

These flow fields are depicted in Figures 19 and 20 for low-drag and high-drag modes, respectively. An excellent agreement for the high-drag mode was obtained with the schlieren photograph of Reference 16. One feature is the existence of a "kink" in the compression wave, which emanates from the impact of the flow with the separation region. This kink was questioned at first, but, when the schlieren photo had been examined carefully, the kink was found easily. Also, all the shock and expansion wave angles (away from the body) were found to be within 4° of the values measured from the schlieren photograph of Reference 16.

The forebody drag coefficient for the high-drag mode was computed as 0.478 (including the 2% increase due to the rotating band) compared to 0.306 for the low-drag case. This represents a 56% increase in drag. The wind tunnel measurement for the high-drag mode was reported¹⁶ to be 0.555. This large discrepancy between the computed and measured values is still unresolved. However, when examining this particular case in Reference 16, the value of 0.555 seems to be particularly high in comparison with the remaining cases tested. The data of Reference 16 for this case were presented with only one point on one figure in the report. There are no cross-checked values or any tabulated results for positive verification of this value. Table 1 provides a summary of all obtained results and a comparison with test data.

5.4 Grid Size Effect. To examine the result obtained for the high-drag mode in Configuration 3, the computations were performed again using a larger number of points to assess whether that

discrepancy was due to inadequate grid size. Configuration 3 was computed first using zones with (15x44), (21x35), and (31x35) points. This grid totals 2,480 points, with a (50x50) mesh equivalence. The grid was then increased to (15x54), (31x45), and (41x45), thus totalling 4,050 points, which is equivalent to a (63x63) mesh. The drag coefficient changed from 0.4621 to 0.4690, a change of only 1.5%. Therefore, it was assumed that the grid size is appropriate for most purposes.

6. SUMMARY AND CONCLUSIONS

Three different spike-nosed projectile configurations were computed at $Mach = 1.72$, and the results are compared to wind tunnel measurements. The computed drag coefficients are in very good agreement with the measured values. Computed values are within 2% of the measurements, which is within the drag-measurement accuracy itself. The high-drag mode computed for the third configuration provided a considerably lower drag than the measured value, although the detailed flow features compared rather accurately with the schlieren photograph of the test. Because confidence was gained from the two previous computed cases, it is believed that the drag measurement for this particular case is quite high and may also be in error. This belief is supported by observing the results of 20 similar spike-nosed configurations tested during the same test period. These drag data are also reported in Reference 16.

Two interesting obstacles are faced in this study which cannot be resolved decisively. First, the possibility of two flow modes always exists. Therefore, one cannot determine, a priori, which mode the numerical procedure will favor. Also, it is not known, a priori, which one will physically occur at particular wind tunnel conditions or under free-flight, firing-range conditions. The second obstacle faced was the strong role of the turbulence eddy viscosity value level and model on influencing the computation (possibly due to the large separation region) toward one particular flow mode. It was not determined whether this influence is purely a numerical problem or it has a parallel in nature where flow turbulence in the tunnel or in free flight may trigger a particular flow mode.

Finally, this study provided a straightforward and systematic capability for computing such difficult configurations. The present work represents an advance in the application of CFD techniques. The computations, in addition, have provided dual flow modes where the wind tunnel experiment had only revealed one mode under certain tunnel conditions. It is not known if some of these computed dual modes are superficial or whether real-life tests had favored only one mode which is more dominant. Thus, these computations may spur the need for extensive and delicate variations in test conditions to verify the existence of these modes at these flow conditions.

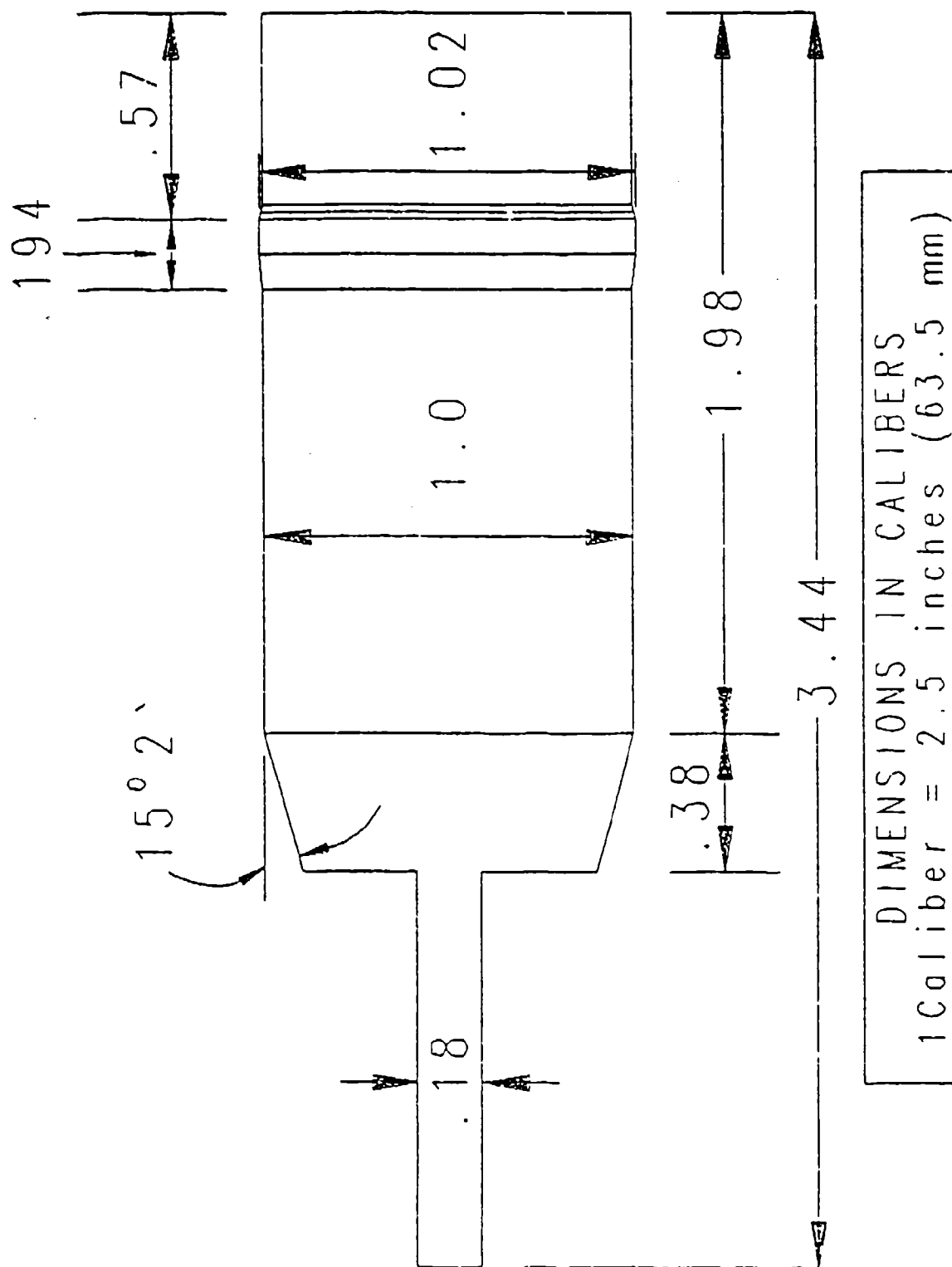
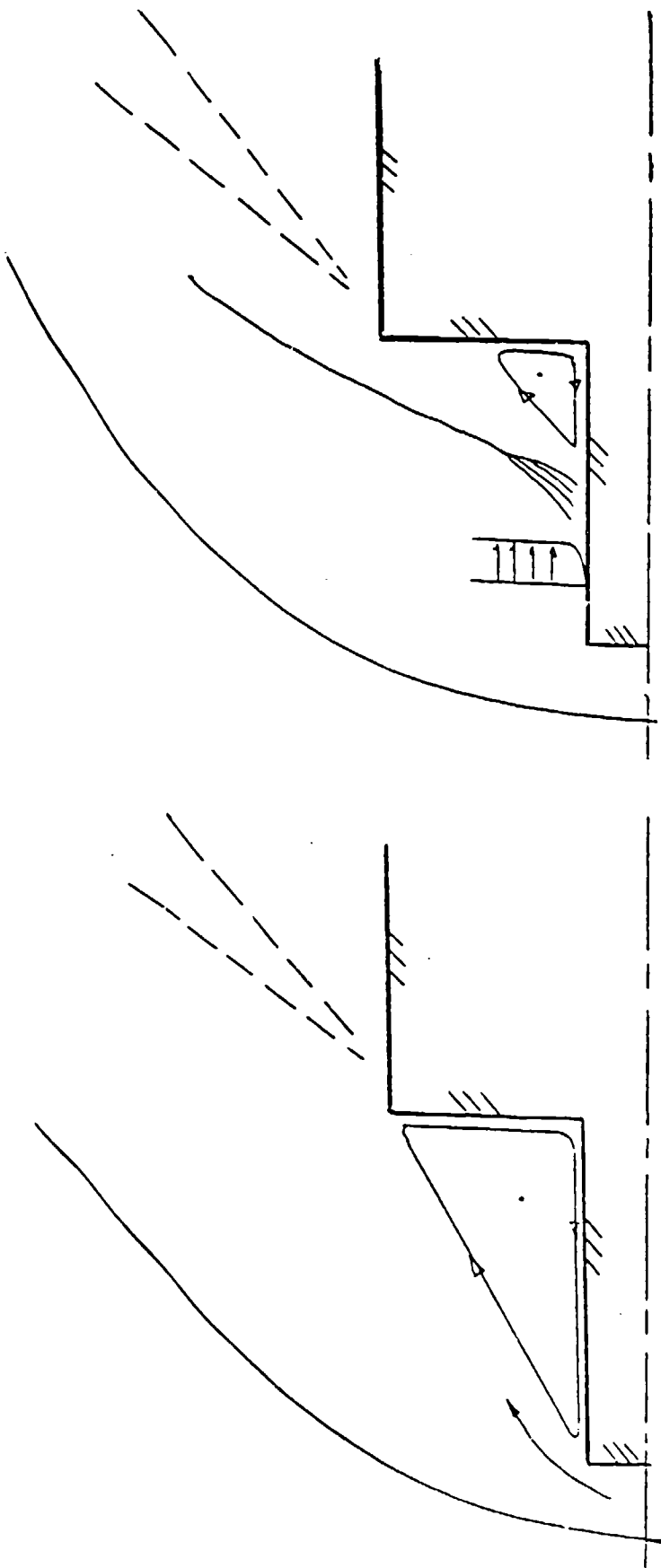


Figure 1. Wind tunnel model of the first projectile configuration.



THE 'CLOSED' FLOW
(LOW - DRAG MODE)

THE 'OPEN' FLOW
(HIGH - DRAG MODE)

Figure 4. Typical flow features for the low- and high-drag modes.

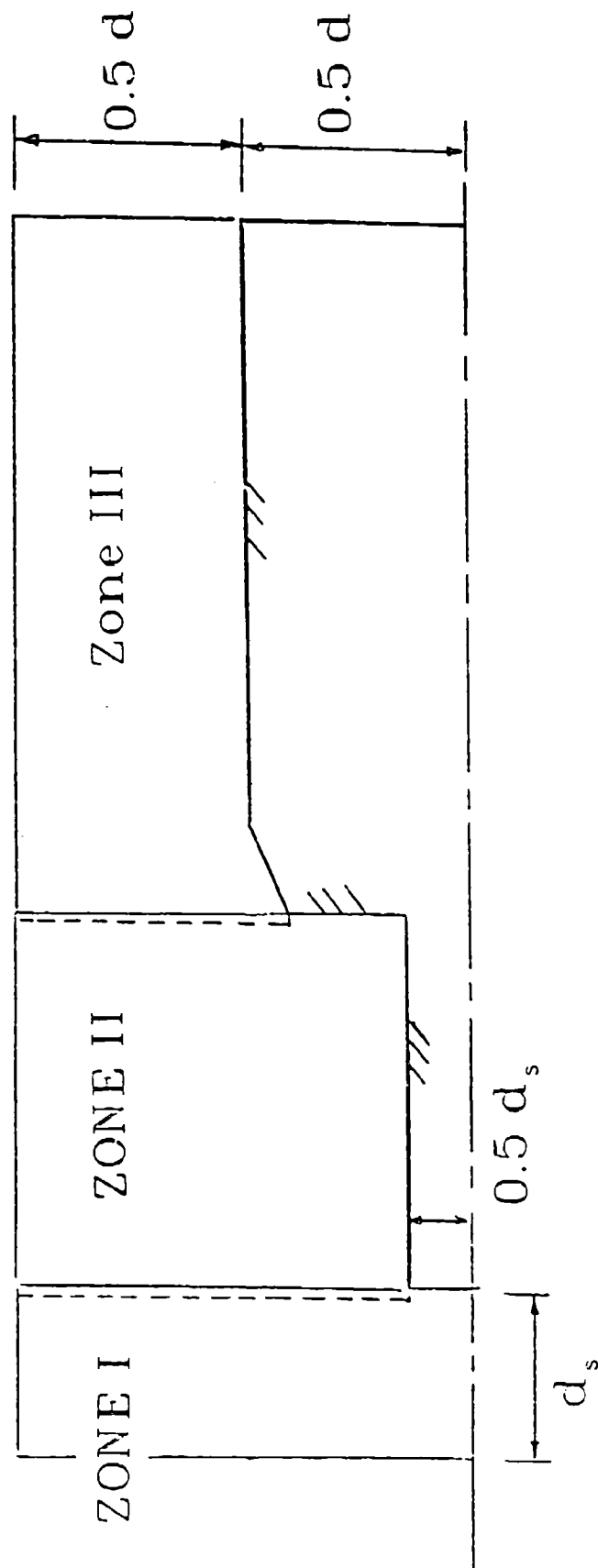


Figure 5. Grid zones and computational domain for the spike-nosed projectiles.

GRID

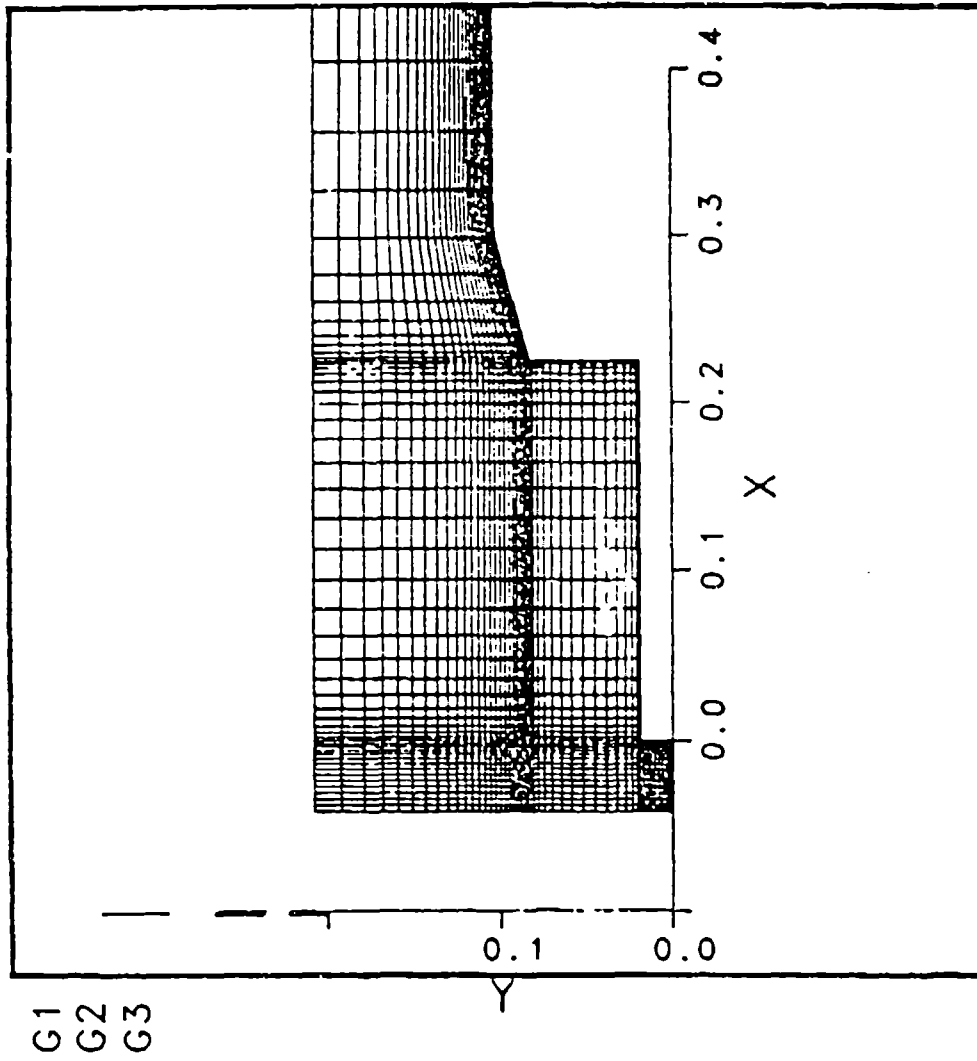
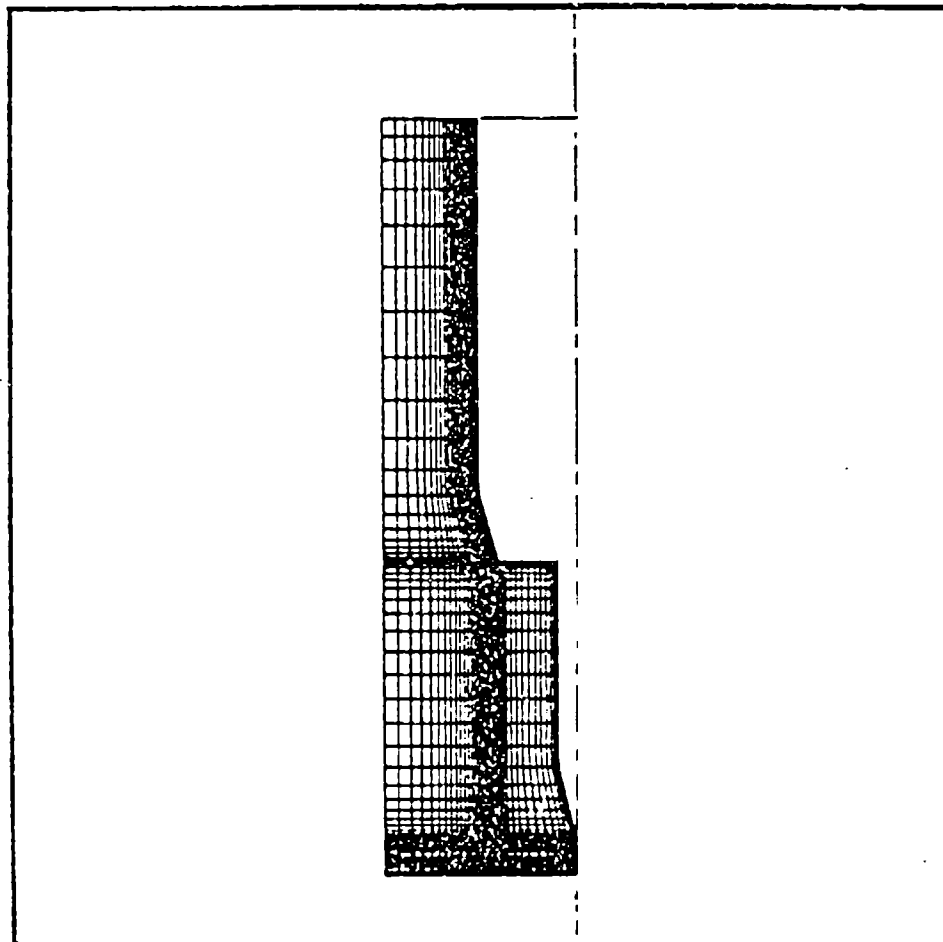


Figure 6. Zonal grid for the first projectile configuration.

GRID



15x39
26x39
21x25

G1
G2
G3

Figure 7. Zonal grid for the second projectile configuration.

GRID

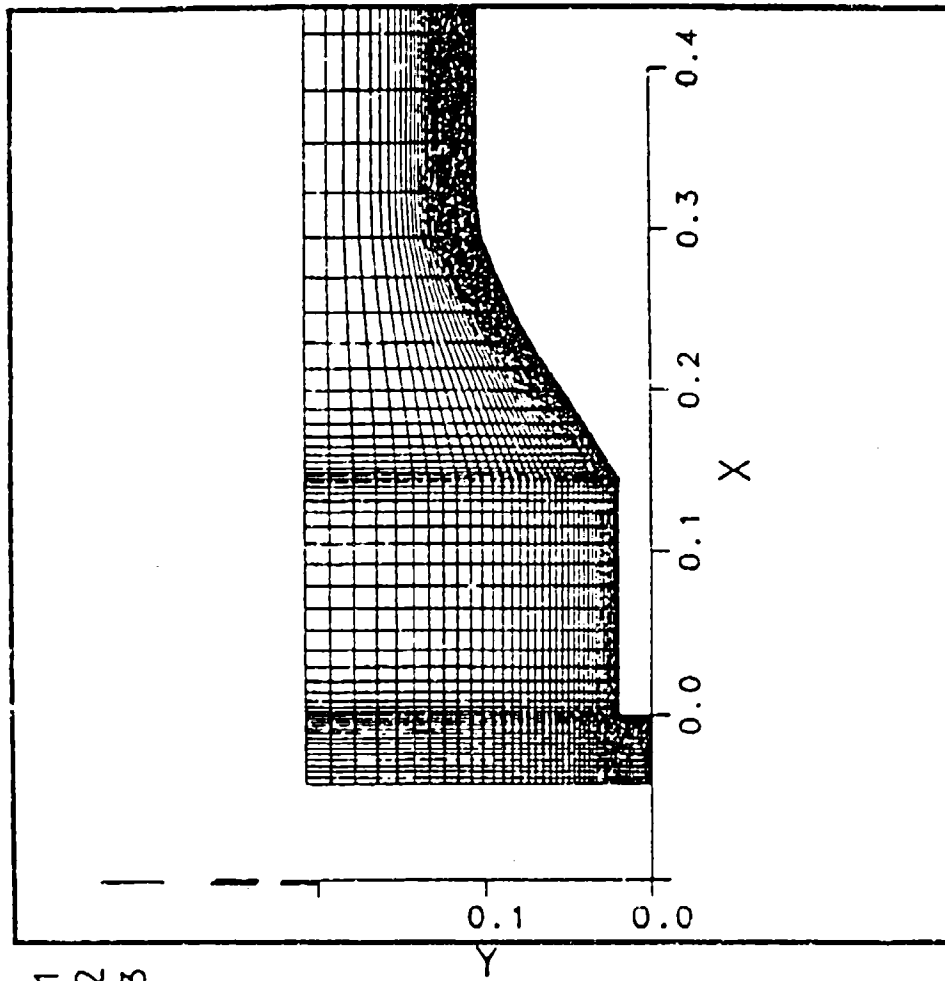


Figure 8. Zonal grid for the third projectile configuration.

MACH NUMBER

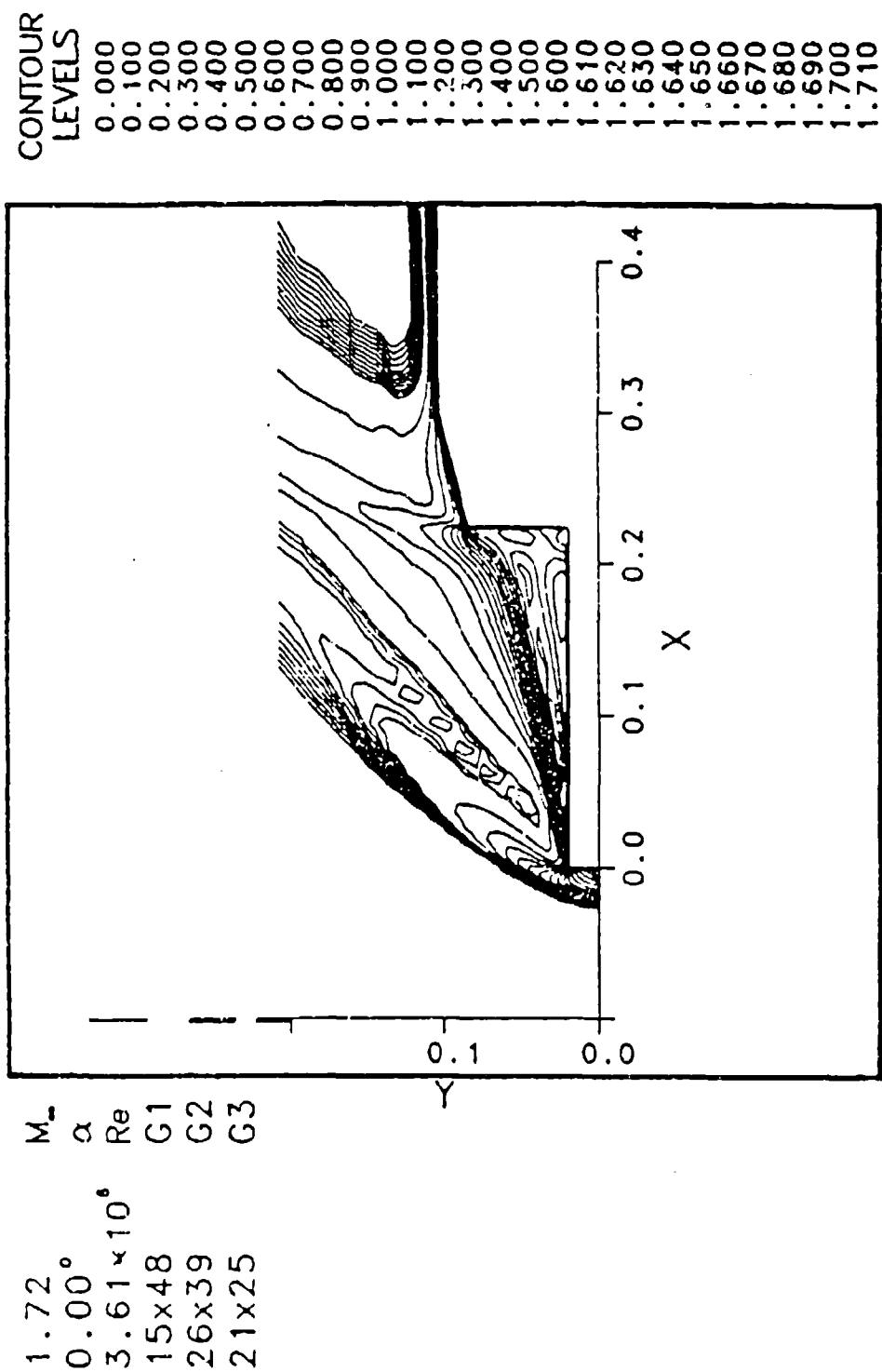


Figure 9. Mach number contours for the low-drag mode for Configuration 1.

MACH NUMBER

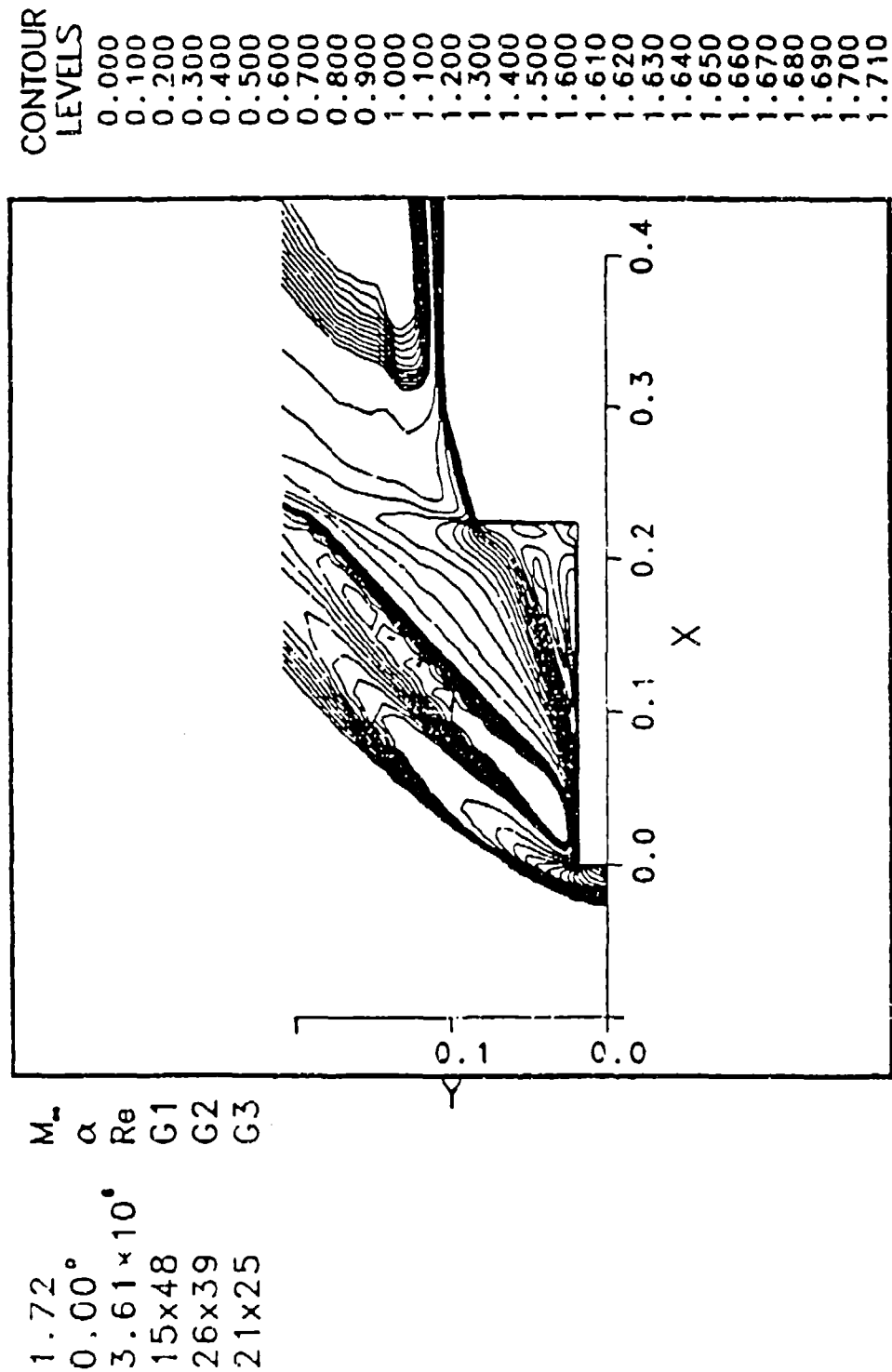
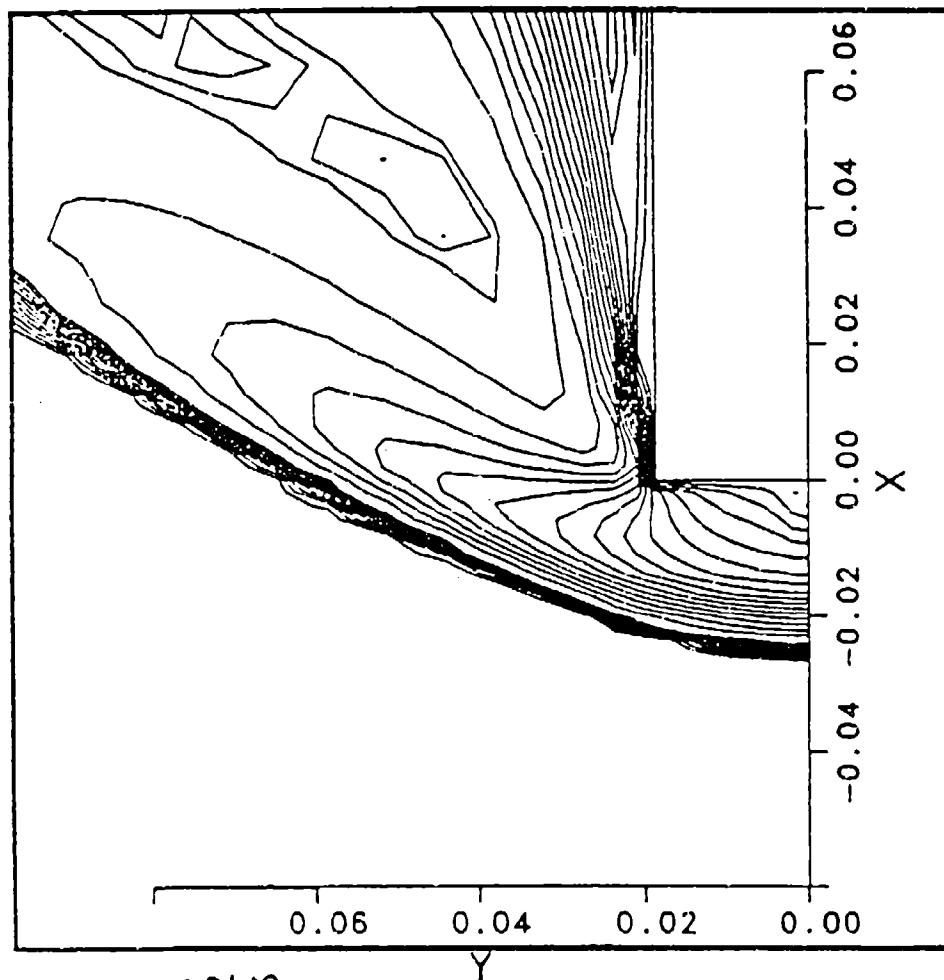


Figure 10. Mach number contours for the high-drag mode for Configuration 1.

MACH NUMBER

CONTOUR
LEVELS

0.000
0.100
0.200
0.300
0.400
0.500
0.600
0.700
0.800
0.900
1.000
1.100
1.200
1.300
1.400
1.500
1.600
1.610
1.620
1.630
1.640
1.650
1.660
1.670
1.680
1.690
1.700
1.710



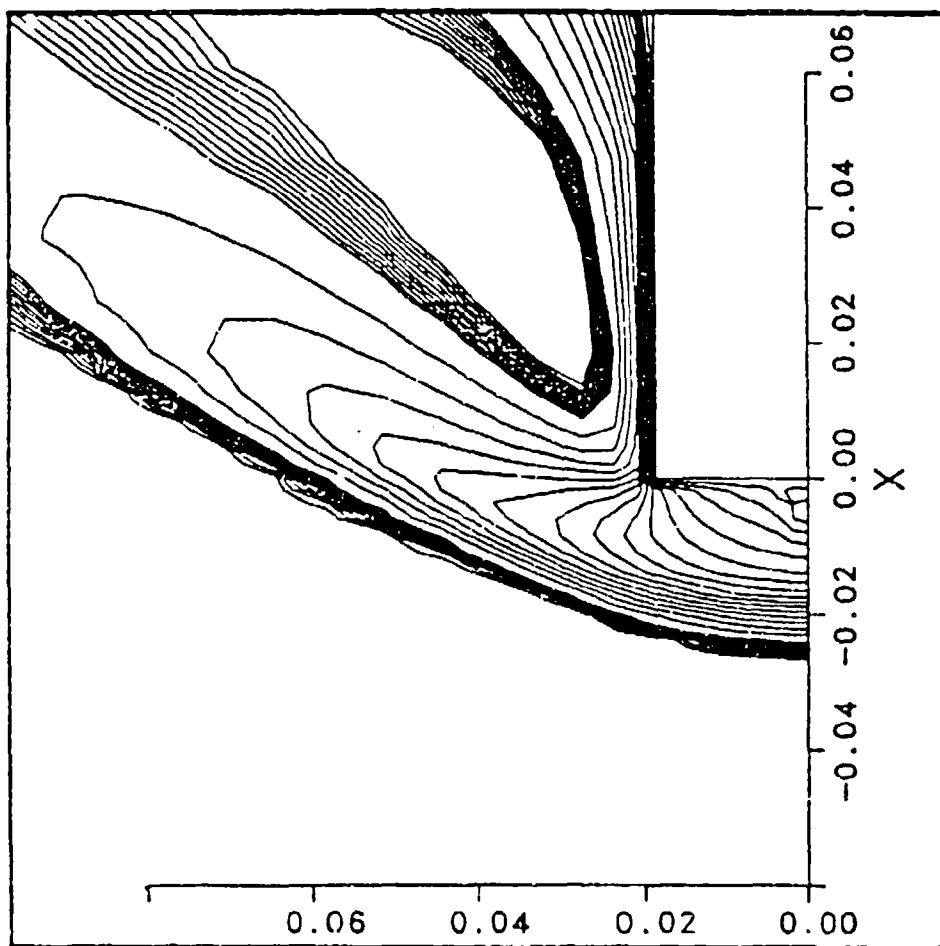
1.72	M_∞
0.00°	α
3.61×10^6	Re
15x48	G1
26x39	G2
21x25	G3

Figure 11. Details of Mach number contours near the spike tip (low-drag, Configuration 1).

MACH NUMBER

CONTOUR
LEVELS

0.000
0.100
0.200
0.300
0.400
0.500
0.600
0.700
0.800
0.900
1.000
1.100
1.200
1.300
1.400
1.500
1.600
1.610
1.620
1.630
1.640
1.650
1.660
1.670
1.680
1.690
1.700
1.710



M_∞	1.72
α	0.00°
Re	3.61×10^6
G1	15x48
G2	26x39
G3	21x25

Figure 12. Details of Mach number contours near the spike tip (high-drag, Configuration 1).

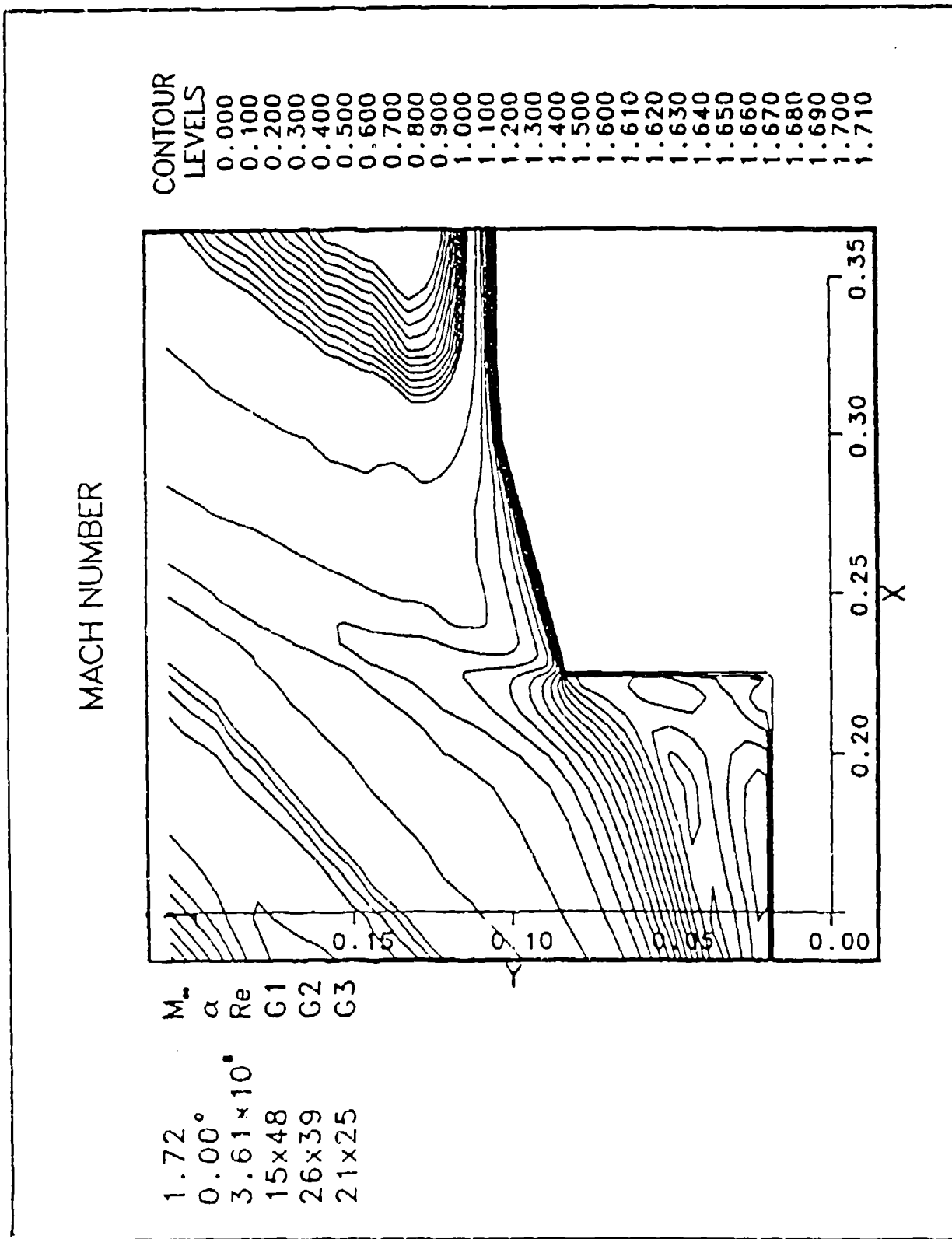
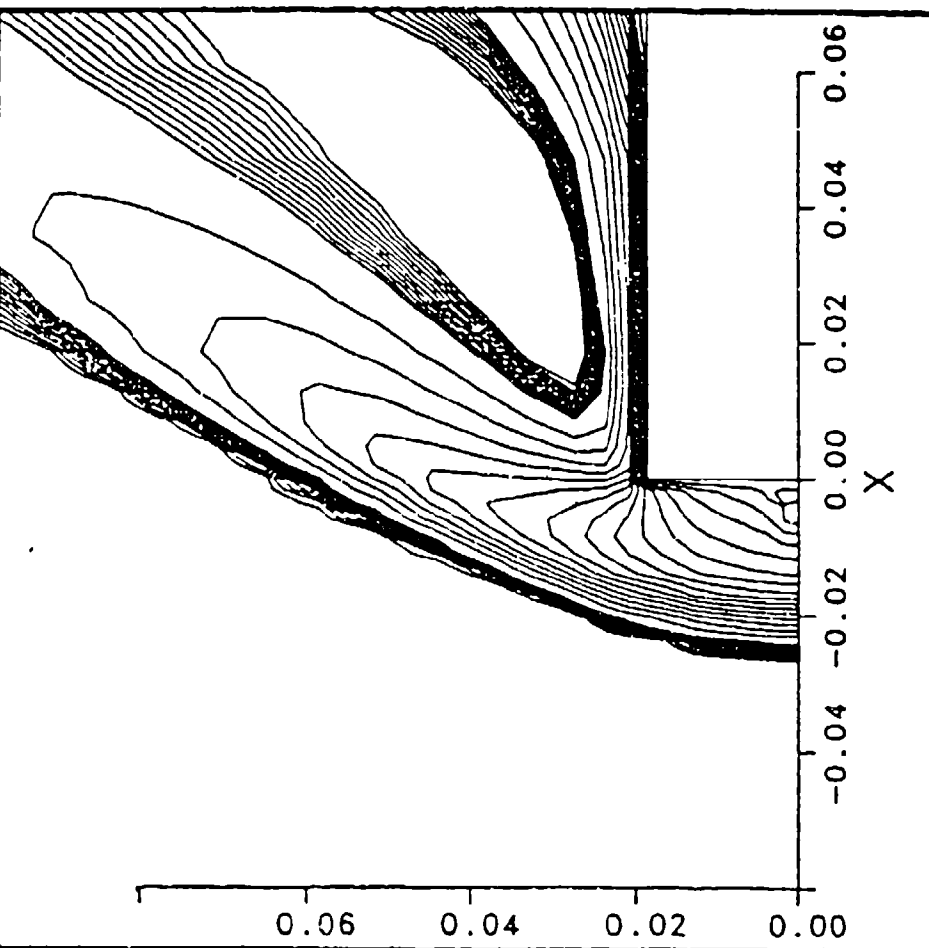


Figure 13. Details of Mach number contours near the facing shoulder (low-drag, Configuration 1D).

MACH NUMBER

M_∞ 1.72
 α 0.00°
 Re 3.61×10^5
 G1 15x48
 G2 26x39
 G3 21x25



CONTOUR
 LEVELS
 0.000
 0.100
 0.200
 0.300
 0.400
 0.500
 0.600
 0.700
 0.800
 0.900
 1.000
 1.100
 1.200
 1.300
 1.400
 1.500
 1.600
 1.610
 1.620
 1.630
 1.640
 1.650
 1.660
 1.670
 1.680
 1.690
 1.700
 1.710

Figure 14. Details of Mach number contours near the facing shoulder (high-drag, Configuration 1).

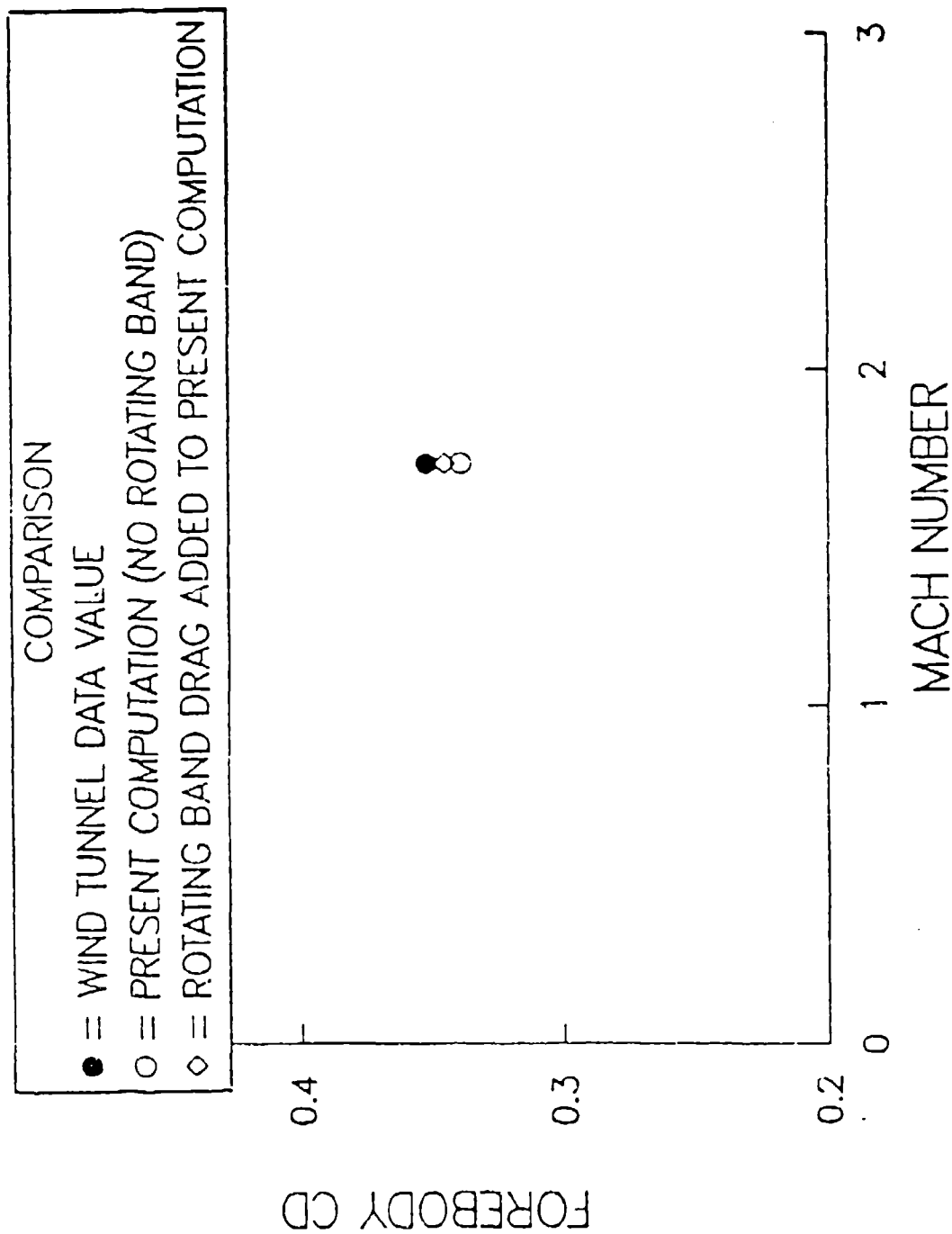


Figure 15. Forebody drag coefficient comparison for Configuration 1 (low-drag mode).

MACH NUMBER

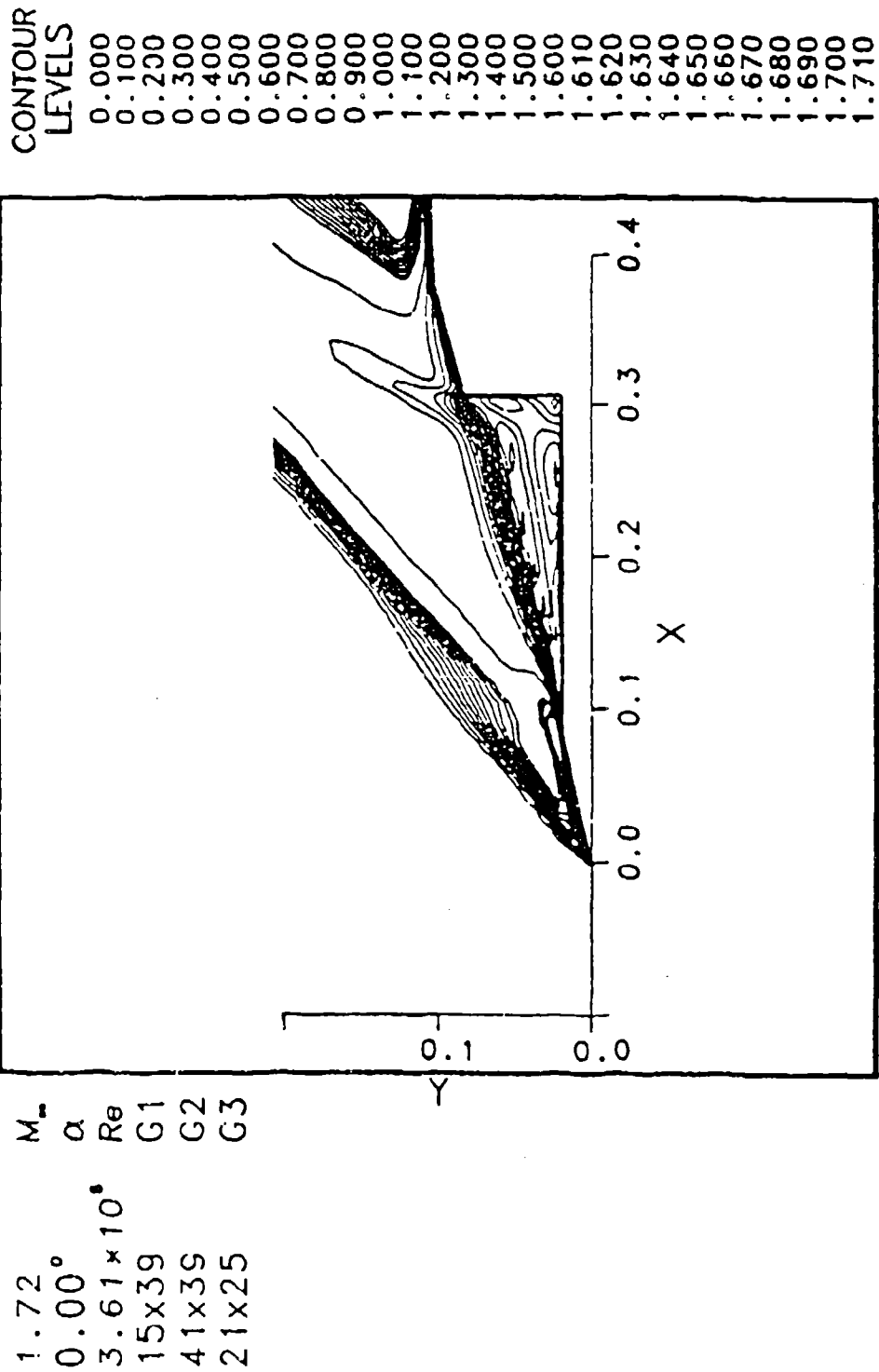


Figure 16. Mach number contours for Configuration 2 (low-drag mode).

MACH NUMBER

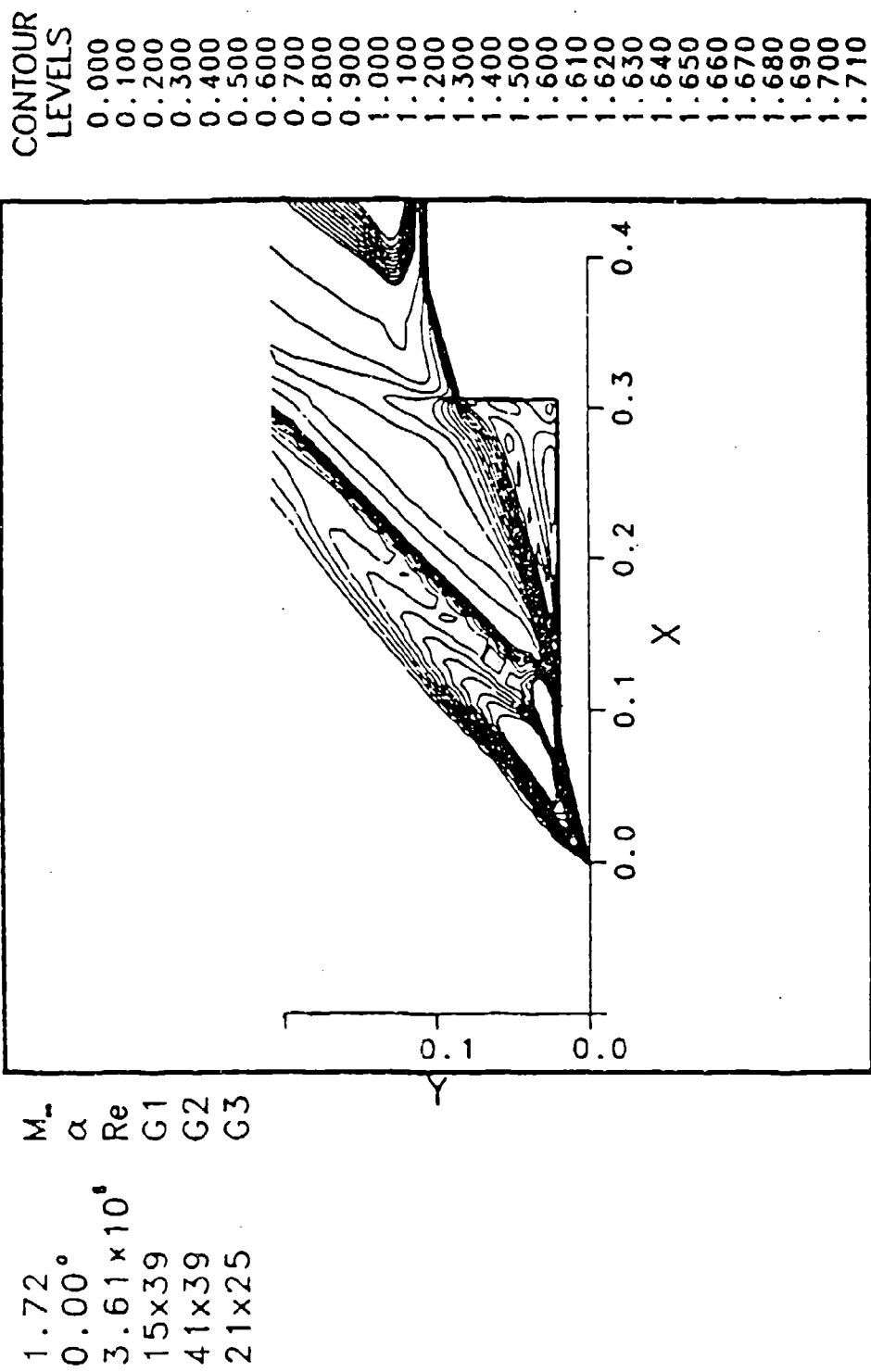


Figure 17. Mach number contours for Configuration 2 (high-drag mode).

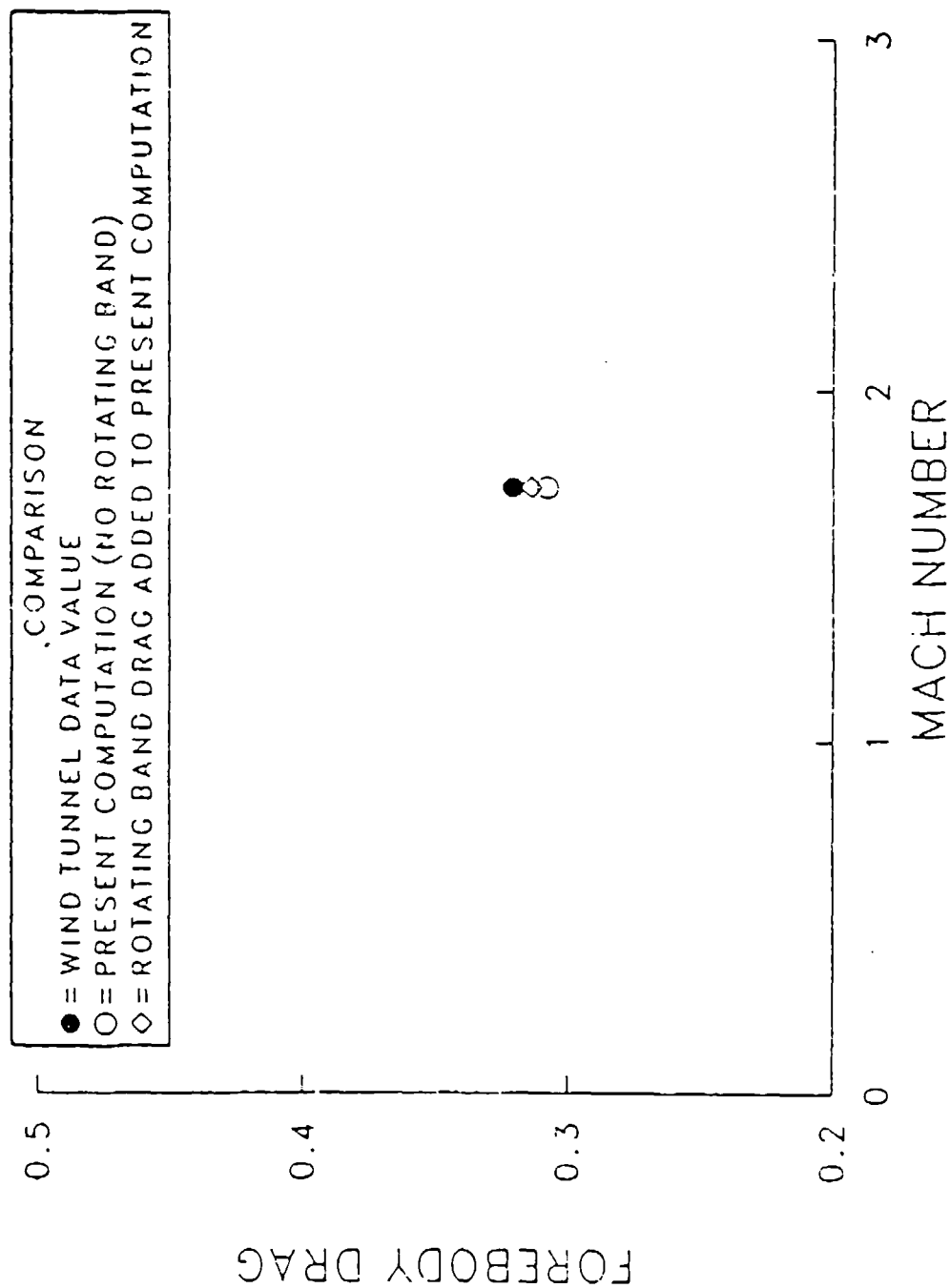


Figure 18. Forebody drag coefficient comparison for Configuration 2 (low-drag mode).

MACH NUMBER

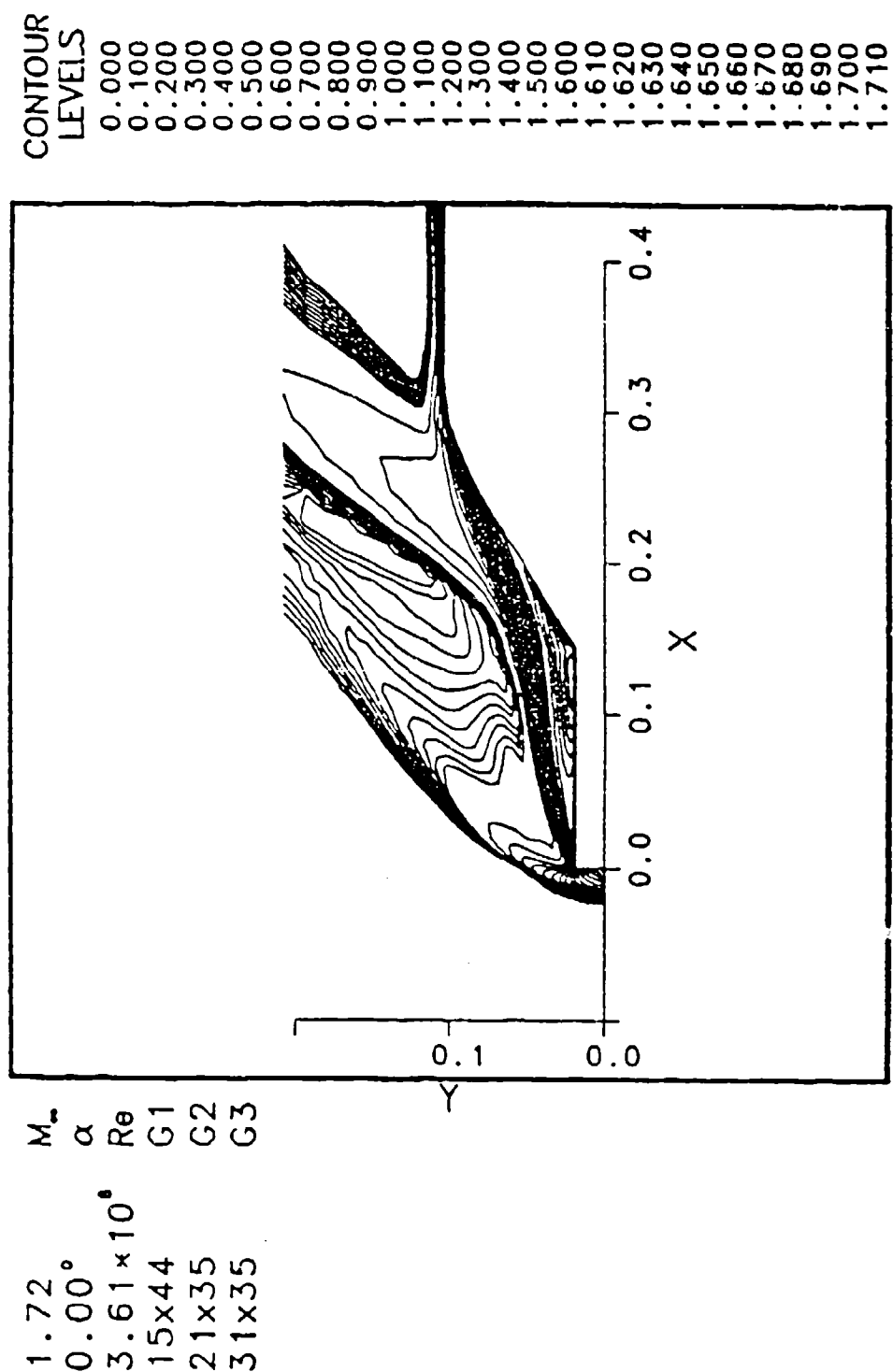


Figure 19. Mach number contours for Configuration 3 (low-drag mode).

MACH NUMBER

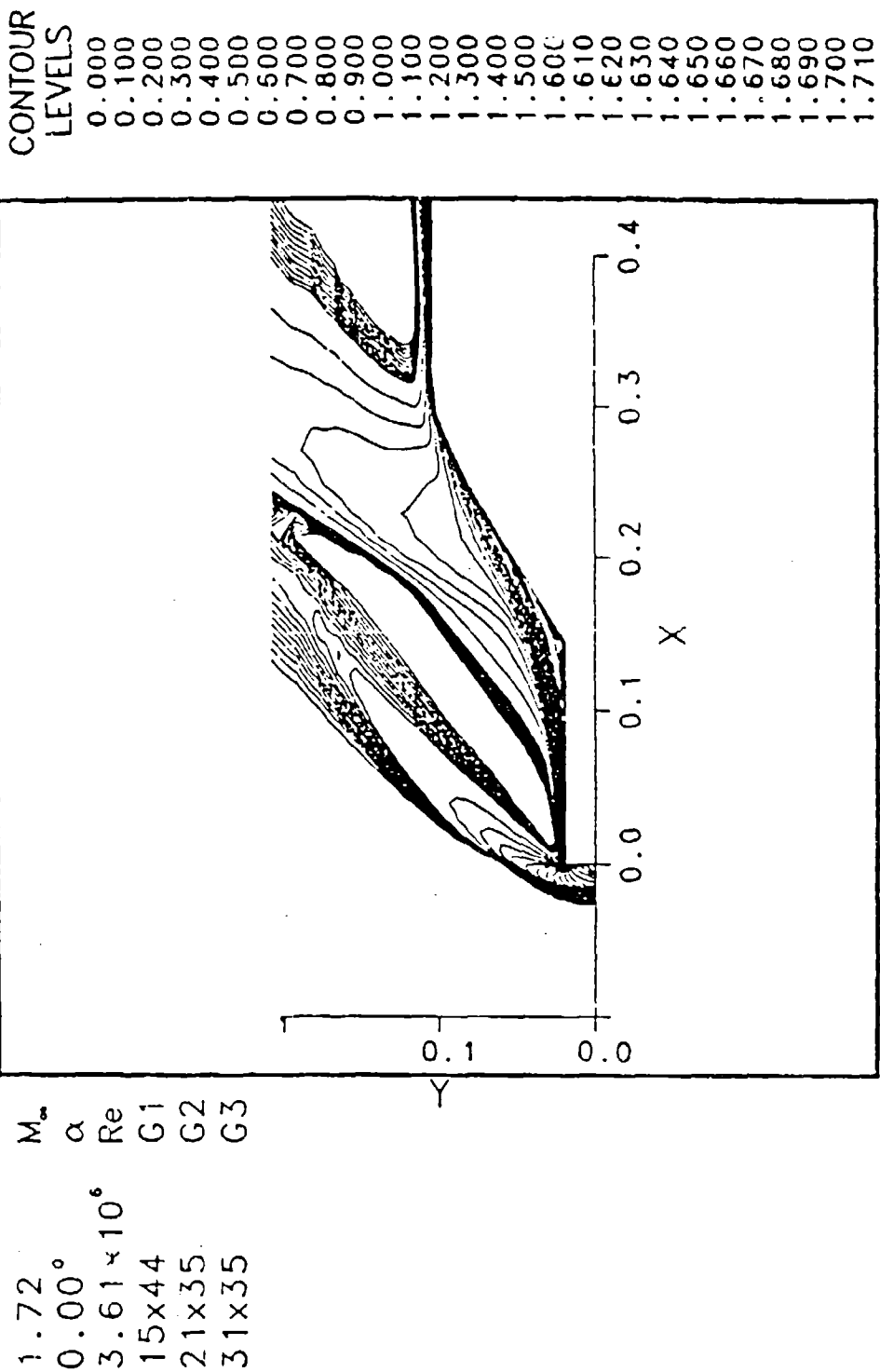


Figure 20. Mach number contours for Configuration 3 (high-drag model).

TABLE 1. Comparison of Results at Mach = 1.72 .

Configuration	C_D			
	Low-Drag Mode		High-Drag Mode	
	Wind Tunnel	Present Computations ^a	Wind Tunnel	Present Computations ^a
1	0.351	0.344	-- ^b	0.410
2	0.321	0.314	-- ^b	0.395
3	-- ^c	0.306	0.555	0.469

^aThese values include an added 2% due to rotating band pressure drag,²² at $M = 1.72$.

^bThis flow mode was not reported in the wind tunnel experiment.¹⁶

^cThis mode was observed and reported only in a schlieren photograph but quickly disappeared and could not be recovered¹⁶ in the wind tunnel for actual measurement.

Intentionally left blank.

7. REFERENCES

1. Krieger, R.H. "Wind Tunnel Test of the T153 120mm HEAT Projectile." BRL-TN-724, U.S. Army Ballistic Research Laboratory, Aberdeen Proving Ground, Maryland, August 1952 (AD 803074).
2. Sylvester, M.A., and Krieger, R.H. "Wind Tunnel Tests of the T340E11 90mm HE Projectile with Varying Spike Nose and Spool-Type-Body Parameters." BRL-MR-1146, U.S. Army Ballistic Research Laboratory, Aberdeen Proving Ground, Maryland, April 1958 (AD 301103).
3. Falkowski, E.W. "Static and Dynamic Stability Characteristics of the Supersonic Infantry Projectile at Transonic Velocities." Technical Memorandum 1565, U.S. Army Picatinny Arsenal, Dover, NJ, June 1965.
4. Falkowski, E.W., and Fleming, G.C. "Aerodynamic Characteristics of the Modified 105-mm M490 Training Projectile." Technical Report ARLCD-TR-81043, ARDC, Dover, NJ, April 1982.
5. Corce, J.D., and Best, J.T. "Static Stability and Axial Force Characteristics of Several U.S. Army 105-mm Antitank Projectile Configurations at Mach Numbers 1.5 to 3.5." AEDC-TR-76-101, Arnold Air Force Station, Tennessee, September 1976.
6. Karpov, B.G., and Piddington, M.J. "Effect on Drag of Two Stable Flow Configurations Over the Nose Spike of the 90mm T316 Projectile." Technical Note No. 595, U.S. Army Ballistic Research Laboratory, Aberdeen Proving Ground, Maryland, October 1954 (AD 803115).
7. Krieger, R.H. "The Aerodynamic Design of Fin Stabilized Ammunition." Memorandum Report No. 971, U.S. Army Ballistic Research Laboratory, Aberdeen Proving Ground, Maryland, February 1956 (AD 90193).
8. Sabin, C.P. "The Aerodynamic Properties of A Spike-Nosed Shell at Transonic Velocities." Memorandum Report No. 1112, U.S. Army Ballistic Research Laboratory, Aberdeen Proving Ground, Maryland, November 1957 (AD 156637).
9. McCoy, R.L. "A Limited Aerodynamic Test of the 105mm Projectile, M456A1, and Three Nose-Spike Modifications." ARBRL-MR-02862, U.S. Army Ballistic Research Laboratory, Aberdeen Proving Ground, Maryland, September 1978 (AD B032242L).
10. Guenther, R.A., and Reding, P.J. "Fluctuating Pressure Environment of A Drag Reducing Spike." AIAA Journal, Vol. 14, No. 12, December 1977, pp. 705-710.
11. Ericsson, L.E. "Flow Pulsation on Concave Conic Forebodies." Journal of Spacecraft and Rockets, Vol. 15, No. 5, September-October 1978, pp 287-292.
12. Reding, P.J., and Jecmen, D.H. "Effects of External Burning on Spike-Induced Separated Flow." Journal of Spacecraft and Rockets, Vol. 20, No. 5, September-October 1983, pp 452-453.
13. Haupt, D.F., and Koenig, K. "Aerodynamic Effects of Probe-Induced Flow Separation on Bluff Bodies at Transonic Mach Numbers." Journal of Spacecraft and Rockets, Vol. 24, No. 4, July-August 1987, pp 327-333.

14. Shang, J.S., Hankey, W.L., and Smith, R.E. "Flow Oscillations of Spike-Tipped Bodies." AIAA Journal, Vol. 20, No. 1, January 1982, pp 25-26.
15. Calarese, W., and Hankey, W.L. "Modes of Shock-Wave Oscillations on Spike-Tipped Bodies." AIAA Journal, Vol. 23, No. 2, February 1985, pp 185-192.
16. Platou, A.S. "Body Nose Shapes for Obtaining High Static Stability." BRL-MR-592, U.S. Army Ballistic Research Laboratory, Aberdeen Proving Ground, Maryland, February 1952 (AD 802157).
17. Unpublished Firing Range Measurements, Launch and Flight Division, U.S. Army Ballistic Research Laboratory, Aberdeen Proving Ground, Maryland, 1980.
18. Koenig, K., Bridges, D.H., and Chapman, G.T. "Transonic Flow Modes of an Axisymmetric Blunt Body." AIAA Paper No. 88-3536, 1st National Fluid Dynamics Congress, Cincinnati, Ohio, July 1988.
19. Patel, N.R., and Sturek, W.B. "Multi-Tasked Numerical Simulation of Axisymmetric Ramjet Flows Using Zonal, Overlapped Grids." BRL-MR-3834, U.S. Army Ballistic Research Laboratory, Aberdeen Proving Ground, Maryland, May 1990 (AD).
20. Baldwin, B.S., and Lomax, H. "Thin-Layer Approximation and Algebraic Model for Separated Turbulent Flows." AIAA Paper No. 78-257, January 1978.
21. Danberg, J.E., and Patel, N.R. "An Algebraic Turbulent Model For Flow Separation Caused by Forward and Backward Facing Steps." BRL-MR-3791, U.S. Army Ballistic Research Laboratory, Aberdeen Proving Ground, Maryland, December 1989 (AD).
22. NSWC-AP Code, Reference: Devan, L. and Mason, L. A. "Aerodynamics of Tactical Weapons to Mach 8 and Angle of Attack 180°: Part II, Computer Program and Users Guide." NSWC-TR-81-358, Naval Surface Weapons Center, Dahlgren, Virginia, September 1981.
23. Whitefield, J.D., and Potter, J.L. "The Influence of Slight Leading Edge Bluntness on Boundary-Layer Transition at Mach Number of Eight." AEDC-TDR-64-18, Arnold Engineering Development Center, Tennessee, March 1964.
24. Sheetz, N. W. "Ballistics Range Experiments on the Effect of Unit Reynolds Number on Boundary-Layer Transition." Proceedings of the 8th Navy Symposium on Aeroballistics, Vol. I, pp. 201-214, June 1969.

LIST OF SYMBOLS

Nomenclature

- A_{ref} = reference area, $(\pi d^2/4)$
 C_D = drag coefficient, drag force/ $(.5 \rho_{\infty} V_{\infty}^2 A_{ref})$
 C_p = specific heat under constant pressure
 C_v = specific heat under constant volume
 d = reference diameter
 d_s = spike diameter
 e = specific total energy
 M = Mach number
 p = static pressure
 Re = Reynolds number
 u, v = velocity components in the x,y directions
 V_{∞} = free stream velocity
 x, y = Cartesian coordinates for 2-D case, axial and radial coordinates for axisymmetric

case

Greek symbols

- α = angle of attack
 γ = ratio of specific heats for air
 ρ = density
 μ = laminar (molecular) viscosity coefficient
 ϵ = turbulent eddy viscosity coefficient
 ξ, η = transformed coordinates in the computational plane for the coordinates x,y

Subscripts

- o = denotes stagnation (total) condition
 ∞ = free stream condition

Intentionally left blank.

No of Copies	Organization
1	Office of the Secretary of Defense OUSD(A) Director, Live Fire Testing ATTN: James F. O'Bryon Washington, DC 20301-3110
2	Administrator Defense Technical Info Center ATTN: DTIC-DDA Cameron Station Alexandria, VA 22304-6145
1	HQDA (SARD-TR) WASH DC 20310-0001
1	Commander US Army Materiel Command ATTN: AMCDRA-ST 5001 Eisenhower Avenue Alexandria, VA 22333-0001
1	Commander US Army Laboratory Command ATTN: AMSLC-DL Adelphi, MD 20783-1145
2	Commander US Army, ARDEC ATTN: SMCAR-IMI-I Picatinny Arsenal, NJ 07806-5000
2	Commander US Army, ARDEC ATTN: SMCAR-TDC Picatinny Arsenal, NJ 07806-5000
1	Director Benet Weapons Laboratory US Army, ARDEC ATTN: SMCAR-CCB-TL Watervliet, NY 12189-4050
1	Commander US Army Armament, Munitions and Chemical Command ATTN: SMCAR-ESP-L Rock Island, IL 61299-5000
1	Commander US Army Aviation Systems Command ATTN: AMSAV-DACL 4300 Goodfellow Blvd. St. Louis, MO 63120-1798

No of Copies	Organization
1	Director US Army Aviation Research and Technology Activity ATTN: SAVRT-R (Library) M/S 219-3 Ames Research Center Moffett Field, CA 94035-1000
1	Commander US Army Missile Command ATTN: AMSMI-RD-CS-R (DOC) Redstone Arsenal, AL 35898-5010
1	Commander US Army Tank-Automotive Command ATTN: AMSTA-TSL (Technical Library) Warren, MI 48397-5000
1	Director US Army TRADOC Analysis Command ATTN: ATAA-SL White Sands Missile Range, NM 88002-5502
(Class. only) 1	Commandant US Army Infantry School ATTN: ATSH-CD (Security Mgr.) Fort Benning, GA 31905-5660
(Unclass. only) 1	Commandant US Army Infantry School ATTN: ATSH-CD-CSO-OR Fort Benning, GA 31905-5660
1	Air Force Armament Laboratory ATTN: AFATL/DLODL Eglin AFB, FL 32542-5000 <u>Aberdeen Proving Ground</u>
2	Dir, USAMSAA ATTN: AMXSY-D AMXSY-MP, H. Cohen
1	Cdr, USATECOM ATTN: AMS/E-TD
3	Cdr, CRDEC, AMCCOM ATTN: SMCCR-RSP-A SMCCR-MU SMCCR-MSI
1	Dir, VLAMO ATTN: AMSLC-VL-D

<u>No. of</u> <u>Copies</u>	<u>Organization</u>	<u>No. of</u> <u>Copies</u>	<u>Organization</u>
4	Commander US Army, ARDEC ATTN: SMCAR-AET-A, R. Kline S. Kahn H. Hudgins J. Grau Picatinny Arsenal, NJ 07306-5000	2	Southwest Research Institute ATTN: Mr. T.R. Jeter Dr. R. White Energetics Systems P.O. Box 28510 San Antonio, TX 78284
2	Commander Naval Surface Warfare Center ATTN: Dr. F. Moore Dr. T. Clare, Code DK20 Dahlgren, VA 22448	1	Battelle Northwest ATTN: Mr. M. Garnich P.O. Box 999 Richland, WA 99358
1	Commander Naval Surface Warfare Center ATTN: Dr. A. Wardlaw Silver Spring, MD 20910	1	Lockheed Company ATTN: Mr. John Gerky P.O. Box 33, Dept. 1/330 Ontario, CA 91761
2	Sandia National Laboratories ATTN: Dr. W.L. Oberkampff Dr. F. Blotner Division 1636 P.O. Box 5800 Albuquerque, NM 87185	1	AAJ Corporation ATTN: Dr. T. Stastney P.O. Box 6767 Baltimore, MD 21204
1	Director NASA Ames Research Center ATTN: MS-227-8, L. Schiff Moffett Field, CA 94035	1	United States Military Academy Department of Mechanics ATTN: LTC Andrew L. Dull West Point, NY 10996
1	Director Defense Advanced Research Projects Agency ATTN: Tactical Technology Office 1400 Wilson Boulevard Arlington, VA 22209	1	Commander US Army Missile Command ATTN: AMSMI-RD, Dr. W. Walker Redstone Arsenal, AL 35898-5000
1	Massachusetts Institute of Technology ATTN: Tech Library 77 Massachusetts Avenue Cambridge, MA 02139		

USER EVALUATION SHEET/CHANGE OF ADDRESS

This Laboratory undertakes a continuing effort to improve the quality of the reports it publishes. Your comments/answers to the items/questions below will aid us in our efforts.

1. BRL Report Number BRL-TR-3140 Date of Report AUGUST 1990

2. Date Report Received _____

3. Does this report satisfy a need? (Comment on purpose, related project, or other area of interest for which the report will be used.) _____

4. Specifically, how is the report being used? (Information source, design data, procedure, source of ideas, etc.) _____

5. Has the information in this report led to any quantitative savings as far as man-hours or dollars saved, operating costs avoided, or efficiencies achieved, etc? If so, please elaborate. _____

6. General Comments. What do you think should be changed to improve future reports? (Indicate changes to organization, technical content, format, etc.) _____

CURRENT
ADDRESS

Name

Organization

Address

City, State, Zip Code

7. If indicating a Change of Address or Address Correction, please provide the New or Correct Address in Block 6 above and the Old or Incorrect address below.

OLD
ADDRESS

Name

Organization

Address

City, State, Zip Code

(Remove this sheet, fold as indicated, staple or tape closed, and mail.)